NSRRC -Jo 5180 (2016)

Polymer Chemistry

PAPER

View Article Online
View Journal | View Issue

Published on 09 December 2015. Downloaded by National Tsing Hua University on 27/06/2016 03:03:47.

Cite this: *Polym. Chem.*, 2016, **7**, 1249

Synthesis, morphology, and electrical memory application of oligosaccharide-based block copolymers with π-conjugated pyrene moieties and their supramolecules†

Han-Sheng Sun,[a] Yougen Chen,[b] Wen-Ya Lee,[c] Yu-Cheng Chiu,[a] Takuya Isono,[b] Toshifumi Satoh,*[b] Toyoji Kakuchi*[b] and Wen-Chang Chen*[a]

Received 20th October 2015,
Accepted 8th December 2015

DOI: 10.1039/c5py01697e

www.rsc.org/polymers

We report the synthesis, morphology, and field effect transistor memory application of maltoheptaose-based block copolymers, maltoheptaose-*block*-poly(1-pyrenylmethyl methacrylate) (MH-*b*-PPyMA), and their supramolecules with (4-pyridyl)-acceptor-(4-pyridyl), MH(4Py-Acceptor-4Py)$_x$-*b*-PPyMA. MH-*b*-PPyMA was prepared by the combination of the *t*-Bu-P$_4$-catalyzed group transfer polymerization and the Cu(I)-catalyzed azide–alkyne cycloaddition reaction. After the thermal annealing process, the MH-*b*-PPyMA bulk sample underwent microphase separation to form the sub-10 nm periodic self-assembled nanostructure. The self-assembled morphologies transform from the hexagonal cylinder packing to the body-centered cubic sphere arrangement and the disordered spherical nanodomain with the increase of the PPyMA segment length. On the contrary, only the spherical nanodomain was observed in the thermo-annealed thin film samples of both MH-*b*-PPyMA and MH(4Py-Acceptor-4Py)$_x$-*b*-PPyMA. The electrical characteristics of the p-type pentacene-based OFET memory device were studied using the thermo-annealed polymer thin film as the electret layer. The MH(4Py-Acceptor-4Py)$_x$-*b*-PPyMA-based organic field effect transistor (OFET) devices had the high hole mobility of 0.20–1.08 cm^2 V^{-1} s^{-1} and the ON/OFF current (I_{ON}/I_{OFF}) ratio of 10^7–10^8, in which the acceptor of the benzo[c][1,2,5]thiadiazole (BT) based device possessed the higher hole mobility than that of the isoindigo-based one due to the more ordered packing pentacene crystals. The memory window (ΔV_{TH}) of the supramolecule-based device was increased with enhancing the 4Py-Acceptor-4Py blending composition, and that of the MH(4Py-BT-4Py)$_{1.5}$-*b*-PPyMA$_{10}$-based device had the largest ΔV_{TH} of *ca.* 9 V, a long-term retention time greater than 10^4 s and the high I_{ON}/I_{OFF} memory ratio of 10^6–10^7 (reading at V_g = 0 V) for more than 100 programming/erasing cycles. Our results demonstrate that the bio-related block copolymers and their supramolecular thin film could be used as electret layers for high-performance nonvolatile flash green memory devices.

Introduction

Organic nonvolatile memory (ONVM) devices have attracted extensive research interest in the electronics field due to the advantages of low cost, light weight, structural flexibility, easy processing, and widespread applications, *e.g.*, RFID, flexible displays, and smart phones.[1,2] Among all the proposed categories of ONVM devices, the organic field-effect transistor (OFET)[3,4] is an emerging and promising device structure for the memory application because of its non-destructive reading behavior, low power consumption, easy integrated structure, and multi-bit storage capability.[5,6] The threshold voltages on transfer curves of the OFET device can be effectively tuned by incorporating an additional charge storage layer, such as ferroelectric materials,[7] polymer electrets,[8–10] and nano-floating gates, into the device as the electret layer.[11–13] For the charge-trapping layers, the polymer electret is a preferred candidate owing to the tunable chemical structure, large-area fabrication, and low-temperature and solution processability. Various polymer electrets have been to date used in transistor memory

[a]*Department of Chemical Engineering, National Taiwan University, Taipei, 10617, Taiwan. E-mail: chenwc@ntu.edu.tw; Tel: +886-2-23628398*
[b]*Division of Biotechnology and Macromolecular Chemistry, Faculty of Engineering, Hokkaido University, Sapporo, 060-8628, Japan.*
E-mail: kakuchi@poly-bm.eng.hokudai.jp, satoh@poly-bm.eng.hokudai.ac.jp; Fax: +81-11-706-6602; Tel: +81-11-706-6602
[c]*Department of Chemical Engineering and Biotechnology, National Taipei University of Technology, Taipei, 10608, Taiwan*
†Electronic supplementary information (ESI) available. See DOI: 10.1039/c5py01697e

Published on 09 December 2015. Downloaded by National Tsing Hua University on 27/06/2016 03:03:47.

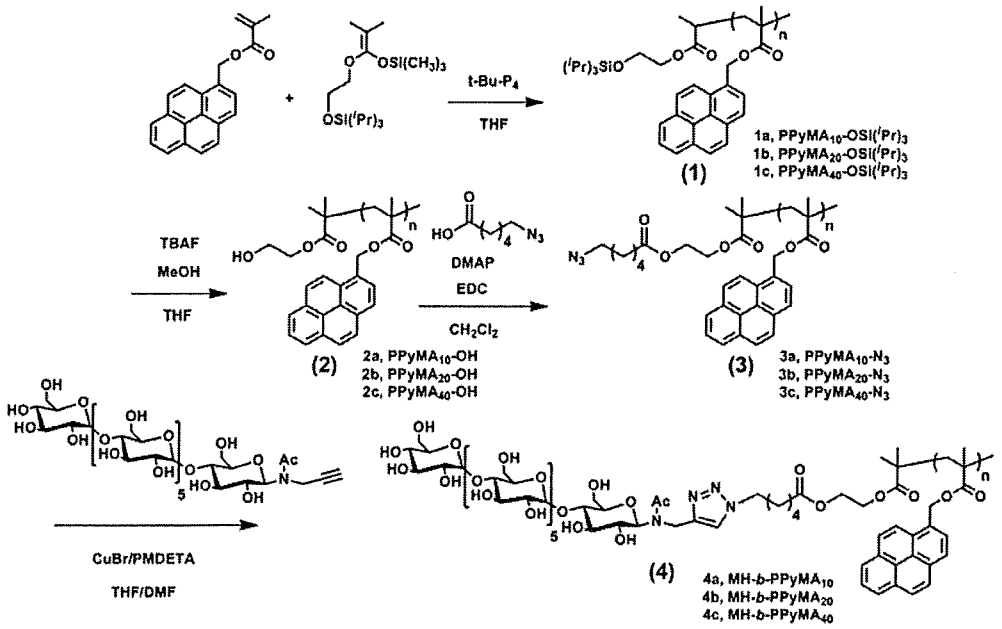

Scheme 1 The synthetic route for MH-*b*-PPyMA diblock copolymers.

devices and the memory characteristics are easily adjustable by the chemical composition, π-conjugation length, polymer architecture, as well as self-assembled morphology.[8,14–17]

In recent years, the concept of green chemistry has been successfully introduced into the electronics field, which points to the innovative utilization of natural resources for electronic applications. For example, green electronics based on carbohydrate polymers are currently becoming increasingly popular due to their environmentally friendly and biocompatible characteristics. Nevertheless, the electron-inactive features of such carbohydrate polymers limit their practical applications in electronics. To improve their electrical properties, the incorporation of an additional electroactive ingredient into the carbohydrate polymers has been proven to be an efficient procedure. For instance, Karakawa *et al.* reported that the carbazolyl-decorated cellulose could be utilized as the electret layer of a resistive memory device, which showed a high ON/OFF current ratio and could be repeatedly operated.[18] In addition to chemical modification, physical blending with graphene oxide[19] or silver nanoparticles[20] also extended the electrical applications of the carbohydrate polymers. Very recently, our group used an oligosaccharide-based diblock copolymer, maltoheptaose-*block*-poly(4-oligofluorenyl styrene) (MH-*b*-PStFl$_n$), as the electret layer of an OFET device and meanwhile demonstrated that the memory characteristics of this device could be manipulated by factors in terms of the fabrication process, the morphology of the electret layer, and the π-conjugation length of the pendent 4-oligofluorenyl side groups.[21] However, obviously, the elucidation of the structural and morphological effects of the "green" polymer electret layer on device memory characteristics is still on the way and should be more profoundly implemented. In particular, the structural effects of the block copolymer based supramolecular complex on the memory behavior have not yet been fully explored.

In this study, we report the syntheses, morphology, and OFET memory characteristics of a maltoheptaose-based block copolymer, maltoheptaose-*block*-poly(1-pyrenylmethyl methacrylate) (MH-*b*-PPyMA, Scheme 1), and its supramolecular complex of MH(4Py-Acceptor-4Py)$_x$-*b*-PPyMA (Scheme S1) (ESI†). The self-assembled nanostructural morphologies of the MH-*b*-PPyMA bulk samples were investigated by small-angle X-ray scattering (SAXS), while the thin film morphologies of MH-*b*-PPyMA and MH(4Py-Acceptor-4Py)$_x$-*b*-PPyMA were examined by atomic force microscopy (AFM) and grazing-incidence small-angle scattering (GISAXS). The electronic characteristics of the MH-*b*-PPyMA and MH(4Py-Acceptor-4Py)$_x$-*b*-PPyMA electret layers were investigated based on the bottom-gate/top-contact OFET memory devices using p-type pentacene as a charge transport layer. In addition, the effect of the incorporating proportion of the 4Py-Acceptor-4Py electron acceptor on OFET memory characteristics was also revealed.

Experimental section

Materials

1-Pyrenecarboxaldehyde (>98.0%), sodium borohydride ($NaBH_4$, >95.0%), methacryloyl chloride (stabilized with MEHQ, >80.0%), diisopropylamine (>99.0%), chlorotriisopropylsilane (>98.0%), chlorotrimethylsilane (>98.0%), propargylamine (>95.0%), tetrakis(triphenylphosphine)palladium(0) ($Pd(PPh_3)_4$, >97.0%), 4-(trimethylstannyl)pyridine (>97.0%),

 This journal is © The Royal Society of Chemistry 2016

Published on 09 December 2015. Downloaded by National Tsing Hua University on 27/06/2016 03:03:47.

6-bromoisatin (>97.0%), and 6-bromooxindole (>98.0%) were purchased from Tokyo Chemical Industry Co., Ltd. Tetrahydrofuran (THF >99.5%), dichloromethane (CH_2Cl_2, >99.5%), triethylamine (NEt_3, >99.0%), *n*-butyllithium (*n*-BuLi, 1.6 M in *n*-hexane), and imidazole (>98.0%) were purchased from Kanto Chemicals Co., Inc. 1-*tert*-Butyl-4,4,4-tris(dimethylamino)-2,2-bis[tris(dimethylamino)-phosphoranylidenamino]-2λ^5,4λ^5-catenadi(phosphazene) (*t*-Bu-P_4, 0.8 M in *n*-hexane), hydrochloric acid (HCl, 37 wt%), sodium hydrocarbonate ($NaHCO_3$, ≥99.7%), tetra-*n*-butylammonium fluoride hydrate (TBAF, 98%), methanol (MeOH, ≥99.9%), 1-ethyl-3-(3-(dimethylamino)propyl)-carbodiimide hydrochloride (EDC, ≥99.0%), sodium (Na, 99.9%), benzophenone (99%), *N*,*N*,*N*′,*N*″,*N*″-pentamethyldiethylenetriamine (PMDETA, 99%), 4-(dimethylamino)pyridine (DMAP, ≥99%), acetic acid (AcOH, ≥99.7%), diethyl ether (Et_2O, ≥99.9%), ethyl acetate (EA, 99.9%), ethanol (EtOH, ≥99.8%), 4,7-dibromo-2,1,3-benzothidiazole (95%), bromine (Br_2, ≥99.5%), potassium carbonate (K_2CO_3, ≥99.0%), 2-octyl-1-dodecanol (97%), triphenylphosphine (PPh_3, 99%), sodium azide (NaN_3, ≥99.5%), 6-bromohexanoic acid (97%), acetic anhydride (Ac_2O, ≥98.0%), calcium hydride (CaH_2, 99.9%), and chloroform ($CHCl_3$, ≥99.9%, stabilized with amylenes) were purchased from Sigma-Aldrich Chemicals Co. Dichloromethane (CH_2Cl_2, 99.9%, extra dry, stabilized), toluene (99.85%, extra dry), *N*,*N*-dimethylformamide (DMF, 99.8%, extra dry), sodium carbonate (Na_2CO_3, 99.6%), magnesium sulfate ($MgSO_4$, anhydrous, 97%), and copper(I) bromide (CuBr, 98%) were purchased from Acros Organics Co. Maltoheptaose (MH) was purchased from Hayashibara Biochemical Lab (Japan). Sublimed pentacene was purchased from Luminescence Technology Corp. (Taiwan). All chemicals were used as received without further purification, unless otherwise noted. THF was refluxed over a sodium wire using benzophenone as an indicator and distilled under an argon atmosphere. 1-Pyrenylmethanol (PyOH),[22] 1-pyrenylmethyl methacrylate (PyMA),[23] 1-(2-triisopropylsiloxyethoxy)-1-trimethylsiloxy-2-methyl-1-propene (TIPS-MTS),[24] 6-azidohexanoic acid,[25] ethynyl-terminated maltoheptaose (ethynyl-terminated MH),[26] 4,7-di(4-pyridyl)-2,1,3-benzothiadiazole (4Py-BT-4Py),[27] and 6,6′-dibromo-*N*,*N*′-bis(2-octyldodecyl)-isoindigo (Br-IID-Br)[28] were synthesized according to previously reported procedures.

Synthesis of trimethylsilyloxy α-end-functionalized PPyMA (PPyMA-OSi^{i}Pr$_3$, 1) by *t*-Bu-P$_4$-catalyzed GTP of PyMA using TIPS-MTS as an initiator. The typical synthetic procedure[29] was as follows: PyMA was first dissolved in dry THF to obtain a 0.6 M solution. Prior to polymerization, the monomer solution was stirred over CaH_2 overnight and then filtered through a 0.45 μm PTFE syringe filter. The polymerization was carried out in a glovebox filled with dry argon (H_2O and O_2, <1 ppm). The preparation of PPyMA$_{10}$-OSi^{i}Pr$_3$ under the initial feed ratio of $[PyMA]_0/[TIPS\text{-}MTS]_0/[t\text{-}Bu\text{-}P_4]_0$ = 10/1/0.004 was taken as an example. TIPS-MTS (50 μL, 0.125 mmol), dry THF (88 μL), and a stock solution of *t*-Bu-P_4 (50 μL, 0.5 μmol, 0.01 M) were sequentially added to a Pyrex® test tube. The mixture was stirred for a few minutes. The PyMA solution (2.08 mL, 1.25 mmol, 0.6 M) was then added dropwise to start the polymerization. After 12 h, a small amount of methanol was added to quench the polymerization. A small proportion of the reaction mixture was sampled to determine the monomer conversion and the residue was reprecipitated twice in a large amount of methanol and washed with hot methanol, followed by drying *in vacuo* to give a yellowish solid (362 mg, 86%). Conversion: 92.0%; $M_{n,GPC}$ = 3300 g mol^{-1}, M_w/M_n = 1.25; $M_{n,NMR}$ = 3070 g mol^{-1}. ^{1}H NMR (400 MHz, $CDCl_3$, δ (ppm)): 8.3–7.2 (broad, aromatic protons), 5.9–4.9 (broad, pyrenyl-C*H*$_2$O$_2$C–), 4.1–3.3 (broad, –SiOC*H*$_2$C*H*$_2$O$_2$C–), 2.2–1.4 (broad, polymer backbone, –C*H*$_2$–), 1.4–1.1 (broad, ((CH$_3$)$_2$C*H*)$_3$SiO–), 1.1–0.3 (broad, ((C*H*$_3$)$_2$CH)$_3$SiO– and polymer backbone, –C*H*$_3$). PPyMA$_{20}$-OSi^{i}Pr$_3$ and PPyMA$_{40}$-OSi^{i}Pr$_3$ were prepared by the same method with different feed ratios. PPyMA$_{20}$-OSi^{i}Pr$_3$: conversion, 96.7%; 420 mg (yield, 91%); $M_{n,GPC}$ = 4890 g mol^{-1}, M_w/M_n = 1.18; $M_{n,NMR}$ = 6150 g mol^{-1}. PPyMA$_{40}$-OSi^{i}Pr$_3$: conversion, 97.6%; 370 mg (yield, 92%); $M_{n,GPC}$ = 7570 g mol^{-1}, M_w/M_n = 1.20; $M_{n,NMR}$ = 12 000 g mol^{-1}.

Synthesis of hydroxyl α-end-functionalized PPyMA (PPyMA-OH, 2). The PPyMA-OH homopolymers were obtained through the deprotection of the triisopropylsilyl group. As a typical method, PPyMA$_{10}$-OSi^{i}Pr$_3$ (300 mg, 0.1 mmol, $M_{n,NMR}$ = 3070 g mol^{-1}) was dissolved in THF (3.0 mL), followed by addition of excess TBAF (654 mg, 2.5 mmol) in THF (5 mL) and methanol (50 μL). The reaction mixture was stirred for 48 h at room temperature, diluted with THF, and passed through a short column of silica gel to remove TBAF. The polymer was purified by reprecipitation into methanol to afford PPyMA$_{10}$-OH as a yellowish solid (231 mg, 81%). ^{1}H NMR (400 MHz, $CDCl_3$, δ (ppm)): 8.3–7.1 (broad, aromatic protons), 5.8–4.9 (broad, pyrenyl-C*H*$_2$OOC–), 4.1–3.6 (broad, –C*H*$_2$OOC– and –O*H*), 3.6–3.4 (broad, –C*H*$_2$OH), 2.2–1.4 (broad, polymer backbone, –C*H*$_2$–), 1.1–0.3 (broad, polymer backbone, –C*H*$_3$). PPyMA$_{20}$-OH (255 mg, 87%) and PPyMA$_{40}$-OH (269 mg, 91%) were prepared under the same reaction conditions.

Synthesis of azido α-end-functionalized PPyMA (PPyMA-N$_3$, 3). As a typical method, a mixture of PPyMA$_{10}$-OH (250 mg, 0.086 mmol, $M_{n,NMR}$ = 2910 g mol^{-1}), 6-azidohexanoic acid (135 mg, 0.86 mmol), DMAP (158 mg, 1.29 mmol), and EDC (247 mg, 1.29 mmol) in dry CH_2Cl_2 (10 mL) was stirred under an argon atmosphere at room temperature. After reacting for 72 h, the reaction solution was concentrated, and then poured into methanol to give PPyMA$_{10}$-N$_3$ as a light yellow solid (249 mg, 95%). ^{1}H NMR (400 MHz, $CDCl_3$, δ (ppm)): 8.3–7.1 (broad, aromatic protons), 5.8–4.8 (broad, pyrenyl-C*H*$_2$OOC–), 4.2–3.6 (broad, –CO$_2$C*H*$_2$C*H*$_2$O$_2$C–), 3.1–2.8 (broad, –C*H*$_2$N$_3$), 2.2–1.4 (broad, –C*H*$_2$CO$_2$– and polymer backbone, –C*H*$_2$–), 1.4–1.1 (broad, –CH$_2$C*H*$_2$(CH$_2$)$_3$CH$_2$CO$_2$–), 1.1–0.3 (broad, polymer backbone, –C*H*$_3$). IR (KBr): 2094 cm^{-1} (–N$_3$ stretching). PPyMA$_{20}$-N$_3$ (249 mg, 97%) and PPyMA$_{40}$-N$_3$ (235 mg, 93%) were prepared under the same reaction conditions.

Synthesis of maltoheptaose-*b*-PPyMA (MH-*b*-PPyMA, 4). The general CuAAC reaction was as follows: PPyMA$_{10}$-N$_3$ (100 mg, 0.033 mmol, $M_{n,NMR}$ = 3050 g mol^{-1}), ethynyl-terminated MH

Published on 09 December 2015. Downloaded by National Tsing Hua University on 27/06/2016 03:03:47.

(81.31 mg, 0.066 mmol), and CuBr (9.47 mg, 0.02 mmol) were placed in a Schlenk flask, evacuated overnight, and then backfilled with argon. The dry THF (2 mL) and DMF (2 mL) were sequentially added to dissolve the $PPyMA_{10}$-N_3 and ethynyl-terminated MH. The degassed PMDETA (22.87 mg, 27.6 μL, 0.132 mmol) was then added. The reaction mixture was placed in an oil bath at 50 °C and vigorously stirred for 72 h. The reaction was monitored by FT-IR until the signal of the azido group totally disappeared. The reaction solution was passed through a short column of silica gel to remove the copper complex and purified by reprecipitation into cold methanol several times in order to wash away the excess ethynyl-terminated MH. The final product of MH-*b*-$PPyMA_{10}$ was obtained as a yellowish solid (120 mg, 85%). ^{1}H NMR (400 MHz, DMF-d_7, δ (ppm)): 8.5–7.4 (broad, aromatic protons), 8.2 (s, proton of the triazole ring), 6.2–3.5 (protons from the maltoheptaose moiety and pyrenyl-CH_2O_2C–), 2.6–0.4 (broad, –CH_2-triazole ring, $-CH_2CH_2(CH_2)_3CH_2COO-$, acetyl, and the polymer backbone, –CH_2– and –CH_3). Anal. calcd for $C_{269}H_{258}N_4O_{60}$: C 71.69%, H 5.77%, N 1.24%; found: C 72.82%, H 5.32%, N 0.88%. MH-*b*-$PPyMA_{20}$ and MH-*b*-$PPyMA_{40}$ were synthesized by a similar method. MH-*b*-$PPyMA_{20}$ (106 mg, 88%). Anal. calcd for $C_{479}H_{418}N_4O_{80}$: C 76.60%, H 5.61%, N 0.75%; found: C 76.59%, H 5.85%, N 0.67%. MH-*b*-$PPyMA_{40}$ (98 mg, 87%). Anal. calcd for $C_{899}H_{738}N_4O_{120}$: C 79.88%, H 5.50%, N 0.41%; found: C 79.40%, H 5.41%, N 0.36%.

Synthesis of 6,6′-di(4-pyridyl)-*N*,*N*′-bis(2-octyldodecyl)-isoindigo (4Py-IID-4Py). A mixture of 6,6′-dibromo-*N*,*N*′-bis(2-octyldodecyl)-isoindigo (880 mg, 0.897 mmol), 4-(trimethylstannyl)-pyridine (478 mg, 1.974 mmol) and tetrakis(triphenylphosphine)palladium(0) ($Pd(PPh_3)_4$, 52 mg, 0.045 mmol) in dry toluene/DMF (12 mL/12 mL) was stirred and refluxed under an argon atmosphere at 100 °C for 60 h. The mixture was cooled to room temperature, and then poured into deionized water. The organic layer was extracted with $CHCl_3$, washed with saturated Na_2CO_3 solution and brine, and dried over $MgSO_4$. After evaporating $CHCl_3$ under reduced pressure, the crude product was further purified by column chromatography over silica gel using $CHCl_3$/EA as the eluent to give 6,6′-di(4-pyridyl)-*N*,*N*′-bis(2-octyldodecyl)-isoindigo as a deep-red solid (438 mg, 50% yield). ^{1}H NMR (400 MHz, CD_2Cl_2, δ (ppm)): 9.25–9.23 (d, 2H), 8.60–8.59 (dd, 4H), 7.48–7.47 (dd, 4H), 7.28–7.25 (dd, 2H), 6.98 (d, 2H), 3.66–3.64 (dd, 4H), 1.89 (m, 2H), 1.30–1.14 (m, 64H) and 0.79–0.74 (m, 12H). ^{13}C NMR (100 MHz, CD_2Cl_2, δ (ppm)): 168.74, 150.99, 147.78, 146.74, 142.37, 133.49, 131.09, 122.93, 121.79, 121.11, 106.89, 45.08, 36.85, 32.49, 32.47, 32.26, 30.59, 30.21, 30.16, 29.93, 29.90, 27.08, 23.26 and 14.46. The NMR spectra on preparing this compound are shown in Fig. S1 and S2 of the ESI.†

Sample preparation for morphological analysis

Firstly, MH-*b*-PPyMA was dried under vacuum for 1 day at room temperature, and then dissolved in chloroform to form a 5 mg mL^{-1} polymer solution. The polymer solution was placed in 1 ml Teflon beakers to evaporate the solvent slowly at room temperature for several days to obtain the bulk samples. The bulk sample was then thermo-annealed under vacuum at 160 °C for 72 h.

For the preparation of the supramolecular complex of MH (4Py-Acceptor-4Py)$_x$-*b*-PPyMA, 4Py-Acceptor-4Py was first dissolved in $CHCl_3$ to form the stock solution (1 mg mL^{-1}). Thereafter, the desired amount of 4Py-Acceptor-4Py solution was added dropwise to the MH-*b*-PPyMA polymer solution, followed by stirring for 7 days at room temperature.

Polymer thin films were prepared by spin-coating the MH-*b*-PPyMA (or MH(4Py-Acceptor-4Py)$_x$-*b*-PPyMA) solution onto 100 nm SiO_2-coated silicon wafers at a spinning rate of 2000 rpm for 60 s. The film thickness was measured using a Filmetrics F20 interferometer or a Surfcorder ET3000 profilometer (Kosaka Lab). The thickness of all polymer thin films was controlled around 50 nm. After spin-coating, the thin films were dried and thermo-annealed under vacuum at 160 °C for 24 h.

Fabrication of the OFET memory device

The highly doped n-type silicon wafer was used as the substrate. A 100 nm thick SiO_2 layer as a gate dielectric was thermally grown onto the silicon substrates. The substrate was pre-cleaned by an ultrasonic cleaning process with toluene, acetone, and isopropanol successively for 20 min each and dried with a steam of nitrogen. The MH-*b*-PPyMA (or MH(4Py-Acceptor-4Py)$_x$-*b*-PPyMA) solution was filtered through a PTFE membrane syringe filter with the pore size of 0.22 μm and spin-coated onto the wafer substrate at 2000 rpm for 60 s. After that, the polymer thin film was dried under vacuum (10^{-7} Torr) at 90 °C for 1 h to remove residual solvents. The thickness of the obtained polymer film was around 50 nm. The 50 nm thick pentacene film was thermally deposited at a deposition rate of 0.4–0.5 Å s^{-1} and a substrate temperature of 90 °C under vacuum (10^{-7} Torr). The 70 nm thick gold source and drain electrodes were subsequently deposited by thermal deposition through a regular shadow mask. The channel length (L) and width (W) were 50 and 1000 μm, respectively. The current–voltage characteristics of the devices were measured by using a Keithley 4200-SCS semiconductor parameter analyzer in a N_2-filled glovebox.

Characterization

The number-average molecular weight ($M_{n,GPC}$) and molecular weight distribution (M_w/M_n) of the prepared polymers were determined by gel permeation chromatography (GPC) using a Lab Alliance RI2000 instrument equipped with Waters Styragel® HR2 and HR4 THF 7.8 × 300 mm columns and a refractive index detector. THF was used as the eluent solvent at a flow rate of 1 ml min^{-1} at 40 °C. $M_{n,GPC}$ and M_w/M_n were calculated on the basis of a calibration using polystyrene standards. The ^{1}H NMR measurements were recorded on a Bruker Avance DRX 400 MHz FT-NMR system. FT-IR spectra were recorded at room temperature using a Perkin-Elmer 100 Model FT-IR spectrophotometer. Samples were cast

 This journal is © The Royal Society of Chemistry 2016

Published on 09 December 2015. Downloaded by National Tsing Hua University on 27/06/2016 03:03:47.

on KBr pellets and scanned 16 times at a resolution of 4 cm^{-1}. The CHN elemental analysis was performed using the "Elementar Vario EL cube" elemental analyzer (for NCSH, Germany). Thermogravimetric analysis (TGA) was performed on a TA Q50 TGA. 3–5 mg powder samples were heated under flowing nitrogen (flow rate 100 cm^3 min^{-1}) at a heating rate of 10 °C min^{-1} from room temperature to 800 °C. The glass transition temperatures (T_gs) were determined using a TA Instrument DSC Q100 at a heating rate of 5 °C min^{-1} from −30 to 250 °C.

UV-Vis absorption spectra were recorded on a Hitachi U-4100 spectrophotometer. For the thin film spectra, polymers were first dissolved in chloroform (5 mg mL^{-1}), followed by filtering through a PTFE membrane syringe filter with a pore size of 0.22 μm, and then spin-coated onto a quartz substrate at a spinning rate of 2000 rpm for 60 s. Cyclic voltammetry (CV) was performed on a CHI 611D electrochemical analyzer using a three-electrode cell in which ITO (polymer film areas were about 0.5 × 0.7 cm^2) was used as a working electrode. A platinum wire was used as an auxiliary electrode. All cell potentials were obtained with the use of a Ag/Ag^+ (0.01 M $AgNO_3$ in acetonitrile) reference electrode. The electrochemical properties of the polymer films were measured in a 0.1 M dry acetonitrile solution containing tetra-*n*-butylammonium perchlorate as the electrolyte. Atomic force microscopy (AFM) imaging was performed on a MultiMode AFM system with a Nanoscope 3D controller (Digital Instruments) in a tapping mode. The spring constant of the silicon cantilevers (Nanosensor PPP-SEIHR) was 15 N m^{-1} (or 42 N m^{-1}) and the resonant frequency was 130 kHz (or 330 kHz). The thickness of the polymer film was measured with a Microfigure Measuring Instrument (Surfcorder ET3000, Kosaka Laboratory Ltd) or a Filmetrics F20 interferometer. The small angle X-ray scattering (SAXS) measurements were performed on the beamline BL 23A1 in the National Synchrotron Radiation Research Center (NSRRC), Taiwan. A monochromatic beam of λ = 0.887 Å (14 keV) was used.[30] SAXS spectra were collected on a Pilatus 1M detector with an area of 169 mm × 179 mm (981 pixels × 1043 pixels). The 1-D scattering intensity profiles were obtained by circularly averaging the 2-D pattern and are reported as the plots of scattering intensity I *versus* the scattering vector q, where $q = (4\pi/\lambda)\sin(\theta/2)$, λ is the wavelength of incident X-rays, and θ is the scattering angle. Grazing incidence small-angle X-ray scattering (GISAXS) data were also collected on the beamline BL23A1 in NSRRC, with a wavelength of 0.827 Å (15 keV) at an incident angle of 0.15°. Grazing incidence wide-angle X-ray scattering (GIWAXS) data were conducted on the beamline BL13A1 in NSRRC. The 12 keV X-ray (wavelength of 1.0219 Å) and an incident angle of 0.20° were used. The 2-D pattern was recorded on a circular Mar 165 CCD (diameter: 165 mm, 1024 pixels × 1024 pixels) detector. The samples were prepared on 1.8 cm × 1.2 cm Si wafer substrates. The capacitance of the bilayer dielectrics was measured on the MIS structure using a Keithley 4200-SCS equipped with a digital capacitance meter (model 4210-CVU).

Results and discussion

Polymer synthesis and chemical structure characterization

The triisopropylsiloxy α-end-functionalized poly(1-pyrenylmethyl methacrylate) (PPyMA-OSi^{i}Pr$_3$) was prepared by the *t*-Bu-P$_4$-catalyzed GTP using TIPS-MTS as the initiator. The monomer conversions are 92.0, 96.7, and 97.6% corresponding to polymerizations under $[PyMA]_0/[TIPS\text{-}MTS]_0$ ratios of 10, 20, and 40, respectively. The yields of the polymer products are as moderate as 91–92%. The chemical transformation from PPyMA-OSi^{i}Pr$_3$ to hydroxyl end-functionalized PPyMA (PPyMA-OH) was implemented by the deprotection of the triisopropylsilyl group of PPyMA-OSi^{i}Pr$_3$ with tetra-*n*-butylammonium fluoride (TBAF), and that from PPyMA-OH to azido end-functionalized PPyMA (PPyMA-N$_3$) was implemented by the esterification of PPyMA-OH with 6-azidohexanoic acid. The Cu(I)-catalyzed azide–alkyne cycloaddition (CuAAC) reaction between PPyMA-N$_3$ and twice the amount of the ethynyl end-functionalized maltoheptaose (MH) was then carried out. After the removal of the residual ethynyl end-functionalized MH by washing with methanol, the pure MH-*b*-PPyMA product was eventually obtained.

The chemical structures of all polymer products are characterized by ^{1}H NMR and FT-IR measurements. The ^{1}H NMR spectra for preparing the MH-*b*-PPyMA diblock copolymer are shown in Fig. 1, as exemplified by MH-*b*-PPyMA$_{10}$. The spectrum of PPyMA-OSi^{i}Pr$_3$s is shown in Fig. 1(a); the broad proton signals are clearly observed in the regions of 8.3–7.2, 5.9–4.9, 2.2–1.4, and 1.1–0.3 ppm due to the aromatic protons, side-chain methylene, backbone methylene, and methyl groups, respectively, together with those due to the TIPS-MTS residue at 4.1–3.3, 1.4–1.1, and 0.85 ppm. After the de-protection of PPyMA-OSi^{i}Pr$_3$s with TBAF, the ^{1}H NMR signals due to the –Si^{i}Pr$_3$ group at 0.85 and 1.4–1.1 ppm completely disappeared (Fig. 1(b)), indicating the successful synthesis of PPyMA-OHs. With the hydroxyl end group transformed to an azido group by reacting PPyMA-OHs with excess 6-azidohexanoic acid (Fig. 1(c)), an obvious shift of the proton peak from 3.5 (–C*H*$_2$OH in PPyMA-OH) to 4.0 (–C*H*$_2$O$_2$CCH$_2$– in PPyMA-N$_3$) ppm and new broad peaks at 3.0 and 1.4–1.1 ppm due to the residue of 6-azidohexanoic acid occurred after the esterification reaction. In addition, the successful preparation of PPyMA-N$_3$s is also adjunctively confirmed by the FT-IR measurements since the characteristic stretching absorption of the azido group clearly appeared at 2094 cm^{-1} after the esterification reaction, as shown in Fig. 2. After the click reaction of PPyMA-N$_3$s with the ethynyl end-functionalized MH, the ^{1}H NMR spectra of the products in Fig. 1(d) simultaneously show the proton signals of MH and PPyMA blocks together with those of the triazole ring at 8.2 ppm, strongly indicating the formation of MH-*b*-PPyMAs. Note that a slight shifting phenomenon of the proton signals toward the upfield region is also observed as previously reported, which is due to the aggregation effect of MH-*b*-PPyMA in DMF-d_7.[21] Additionally, the FT-IR measurements and elemental analyses also support the above inference, *i.e.*, the formation of MH-*b*-

Published on 09 December 2015. Downloaded by National Tsing Hua University on 27/06/2016 03:03:47.

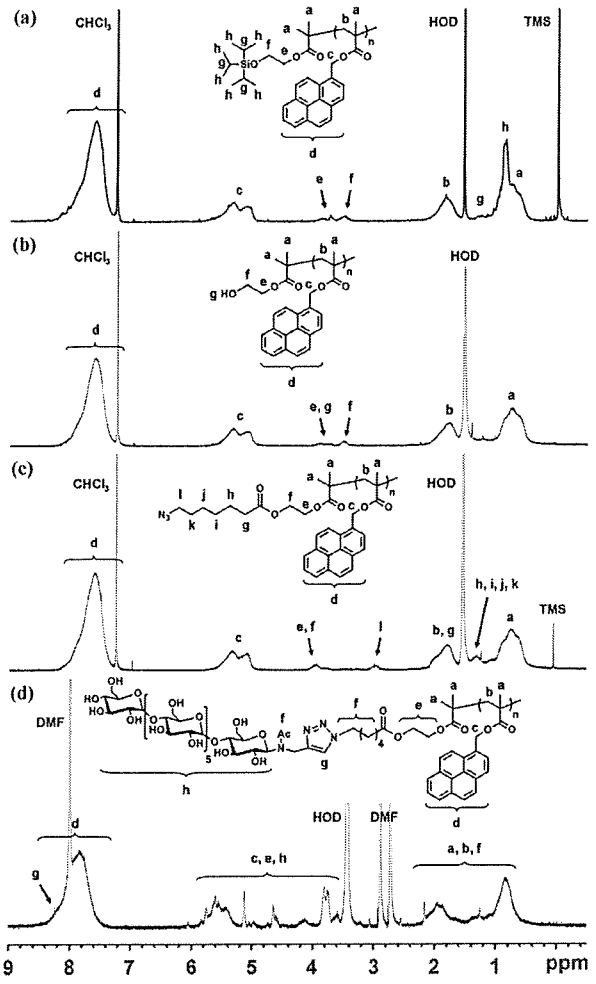

Fig. 1 ^{1}H NMR spectra of (a) PPyMA$_{10}$-OSi^{i}Pr$_3$ in $CDCl_3$, (b) PPyMA$_{10}$-OH in $CDCl_3$, (c) PPyMA$_{10}$-N_3 in $CDCl_3$, and (d) the MH-*b*-PPyMA$_{10}$ diblock copolymer in DMF-d_7.

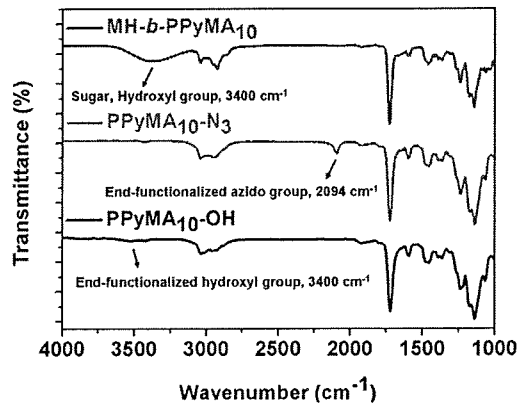

Fig. 2 FT-IR spectra of PPyMA$_{10}$-OH, PPyMA$_{10}$-N_3, and the MH-*b*-PPyMA$_{10}$ diblock copolymer.

PPyMA after the click reaction is accompanied by the complete disappearance of the stretching vibration at 2094 cm^{-1} due to the azido group of PPyMA-N_3 and the new appearance of the absorption band around 3400 cm^{-1} due to the hydroxyl groups of MH. The ^{1}H NMR and FTIR spectra of the MH-*b*-PPyMA with the other block ratios are shown in Fig. S3 and S4 of the ESI,† which also suggest the successful preparation of the polymers. The elemental analysis of the final product indicates that its experimental CHN composition agrees well with the theoretical value of MH-*b*-PPyMA.

Table 1 lists the molecular-weight information of PPyMA-OSi^{i}Pr$_3$ and MH-*b*-PPyMA. The molecular weight of PPyMA-OSi^{i}Pr$_3$ is estimated by both ^{1}H NMR and GPC measurements. The $M_{n,NMR}$s of PPyMA$_{10}$-OSi^{i}Pr$_3$, PPyMA$_{20}$-OSi^{i}Pr$_3$, and PPyMA$_{40}$-OSi^{i}Pr$_3$ are 3070, 6150, and 12 000 g mol^{-1}, each of which is quite consistent with its related $M_{n,theo.}$ of 3050, 6100, and 12 000 g mol^{-1} calculated on the basis of $M_{n,theo.}$ = [PyMA]$_0$/[TIPS-MTS]$_0$ × (M.W. of PyMA, 300.35 g mol^{-1}) × conv. + (M.W. of TIPS-MTS residue, 288.50 g mol^{-1}). The $M_{n,GPC}$ in the range of 3300–7570 g mol^{-1} deviates from the $M_{n,theo.}$, due to the structural mismatch of PPyMA with polystyrene standards. All the GPC traces in Fig. S5 (ESI†) show a unimodal shape and narrow distribution, from which the M_w/M_ns of PPyMA$_{10}$-OSi^{i}Pr$_3$, PPyMA$_{20}$-OSi^{i}Pr$_3$, and PPyMA$_{40}$-OSi^{i}Pr$_3$ are estimated to be 1.25, 1.18, and 1.20, respectively. It is worth mentioning that the molecular weight and M_w/M_n values of PPyMA-OH and PPyMA-N_3 show no significant change with their related PPyMA-OSi^{i}Pr$_3$. The $M_{n,NMR}$s of MH-*b*-PPyMA$_{10}$, MH-*b*-PPyMA$_{20}$, and MH-*b*-PPyMA$_{40}$ are 4290, 7370, and 13 200 g mol^{-1}. Any attempt to carry out the GPC measurements in THF or DMF has failed because of the insoluble issue of MH-*b*-PPyMA.

Thermal properties

The thermal properties of MH, PPyMA-N_3, and MH-*b*-PPyMA were investigated by TGA and DSC measurements, as shown in Fig. 3. Table 1 summarizes all the thermal decomposition temperatures (T_d, onset weight loss temperature) and glass transition temperatures (T_g). In Fig. 3(a), for MH (black line), a clear weight loss prior to 100 °C is observed due to the evaporation of the adsorbed moisture, and its T_d is around 207 °C. PPyMA-N_3s show the initial (onset) thermal degradation in the temperature range of 303–314 °C and then a two-stage thermal degradation in the regions of 280–360 °C and 370–470 °C, which are attributed to the T_ds of the polymer main-chain backbone and the aromatic pyrene side groups, respectively. In addition, a high T_d has been observed for a high molecular-weight PPyMA-N_3, suggesting that the increase of molecular weight of PPyMA-N_3 improves the thermal stability. MH-*b*-PPyMAs exhibit a discriminable two-stage degradation separately located in the regions of 270–340 °C and 350–460 °C, of which the former one coincides with the decomposition curve of MH, while the latter one with that of the PPyMA block. The incorporation of MH with PPyMA leads to the decrease of the T_d value of either block of MH-*b*-PPyMA when compared with each related homopolymer, *i.e.*, the T_d of MH-*b*-PPyMA is

 This journal is © The Royal Society of Chemistry 2016

Published on 09 December 2015. Downloaded by National Tsing Hua University on 27/06/2016 03:03:47.

Table 1 Syntheses and physical properties of $PPyMA_n$-OSi^iPr_3 homopolymers and MH-*b*-$PPyMA_n$ diblock copolymers

Samples	$M_{n,NMR}$ (g mol^{-1})	$M_{n,GPC}$ [c] (g mol^{-1})	M_w/M_n [c]	T_d [d] (°C)	T_g [e] (°C)	*d*-spacing [f] (nm)
$PPyMA_{10}$-OSi^iPr_3 [a]	3070	3300	1.25	303[h]	128[h]	n.a.[g]
$PPyMA_{20}$-OSi^iPr_3 [a]	6150	4890	1.18	314[h]	138[h]	n.a.[g]
$PPyMA_{40}$-OSi^iPr_3 [a]	12 000	7570	1.20	314[h]	139[h]	n.a.[g]
MH-*b*-$PPyMA_{10}$ [b]	4290	n.a.[g]	n.a.[g]	277	147	11.2 (Hex)
MH-*b*-$PPyMA_{20}$ [b]	7370	n.a.[g]	n.a.[g]	282	154	9.3 (BCC)
MH-*b*-$PPyMA_{40}$ [b]	13 200	n.a.[g]	n.a.[g]	282	147	10.9

[a] Estimated by ^{1}H NMR in $CDCl_3$. The number average molecular weight of PPyMA-OSi^iPr_3 was calculated on the basis of the equation: $M_{n,NMR}$ ($PPyMA_n$-OSi^iPr_3) = $[PyMA]_0/[TIPS\text{-}MTS]_0$ × (M.W. of PyMA) × conv. + (M.W. of TIPS-MTS residue). [b] Estimated by ^{1}H NMR in DMF-d_7 and elemental analysis. [c] Measured by GPC using PMMA standards in THF. [d] Onset weight loss temperature determined by TGA at a heating rate of 10 °C min^{-1} under a N_2 atmosphere. [e] Determined by DSC at a heating rate of 5 °C min^{-1} under a N_2 atmosphere. [f] Determined by SAXS measurements using thermo-annealed bulk samples. [g] Not available. [h] Result from PPyMA-N_3.

around 277–282 °C, while that of PPyMA-N_3 alone is around 303–314 °C. The T_gs of MH, PPyMA-N_3, and MH-*b*-PPyMA are measured by DSC at the heating rate of 5 °C min^{-1}, as shown in Fig. 3(b). No obvious T_g is observed for MH. The endothermic peak around 190 °C is due to the caramelization temperature of MH.[31,32] The T_g of PPyMA-N_3 is in the region of 128–138 °C, increasing with the increase of molecular weight of PPyMA-N_3. Compared to PMMA with a T_g of around 100 °C, PPyMA-N_3 shows an obviously higher T_g due to the strong intermolecular interaction between its rigid pyrenyl side groups, *e.g.*, π–π stacking. Interestingly, MH-*b*-PPyMA shows an 8–19 °C higher T_g than its related PPyMA-N_3, which is very likely due to the strong hydrogen bonding caused by MH segments.[33,34]

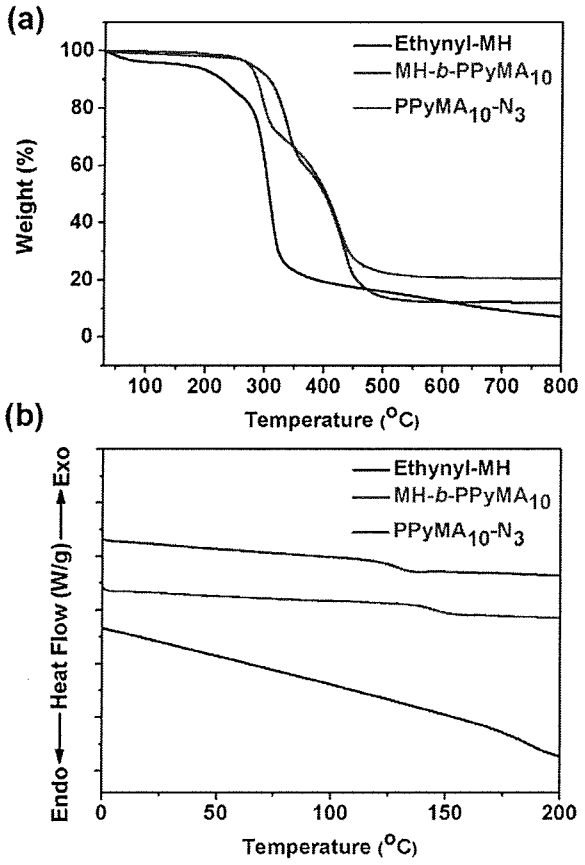

Fig. 3 (a) TGA diagrams and (b) DSC curves of the ethynyl-terminated MH, $PPyMA_{10}$-N_3, and the MH-*b*-$PPyMA_{10}$ diblock copolymer.

Morphology of the bulk sample

The microphase-separation behaviors of the thermo-annealed MH-*b*-PPyMA bulk samples are examined by small-angle X-ray scattering (SAXS) measurements, as shown in Fig. 4. The apparent first-order scattering peaks located at q^* = 0.065, 0.068, and 0.058 Å^{-1} are observed for the thermo-annealed bulk samples of MH-*b*-$PPyMA_{10}$, MH-*b*-$PPyMA_{20}$, and MH-*b*-$PPyMA_{40}$, respectively. Apart from the first-order scattering peak, the higher order scattering patterns of $q/q^* = \sqrt{3}, 2, \sqrt{7}$ and $q/q^* = \sqrt{2}, \sqrt{3}$ are also observed for the MH-*b*-$PPyMA_{10}$ and MH-*b*-$PPyMA_{20}$ bulk samples, respectively, from which the microphase-separation nanostructure can be presumed to be a closely-packed hexagonal (Hex) cylinder for MH-*b*-$PPyMA_{10}$ and a body-centered cubic (BCC) sphere for MH-*b*-$PPyMA_{20}$ bulk samples. The unclear higher order peak of MH-*b*-$PPyMA_{40}$ is due to the longer chain length of the PPyMA block, which decreases the Flory–Huggins interaction χ and mixing free energy, resulting in the poorer arrangement and indistinct assembled structure. The average *d*-spacings ($d_{MH\text{-}b\text{-}PPyMA_n}$, center-to-center distance) calculated on the basis of Bragg's formula ($d = 4\pi/\sqrt{3}q^*$ for a Hex cylinder and $d = 2\pi/q^*$ for BCC and a random sphere) are 11.2, 9.3, and 10.9 nm for the corresponding bulk samples, respectively. The *d*-spacing of the BCC structure increases reasonably with enhancing the chain length of the $PPyMA_n$ block from n = 20 to 40, while that of $d_{MH\text{-}b\text{-}PPyMA_{10}}$ is abnormally higher than the other two samples. As previously reported,[35] the domain size of the self-assembled MH (d_{MH}) is about 5 nm, from which the domain size of the $PPyMA_n$ block (d_{PPyMA_n}) can be roughly estimated by using the equation $d_{PPyMA_n} = d_{MH\text{-}b\text{-}PPyMA_n} - d_{MH}$. Surprisingly, the size of the $PPyMA_{10}$ domain is accordingly estimated to be ~6.2 nm. This value is much greater than those of $PPyMA_{20}$

Published on 09 December 2015. Downloaded by National Tsing Hua University on 27/06/2016 03:03:47.

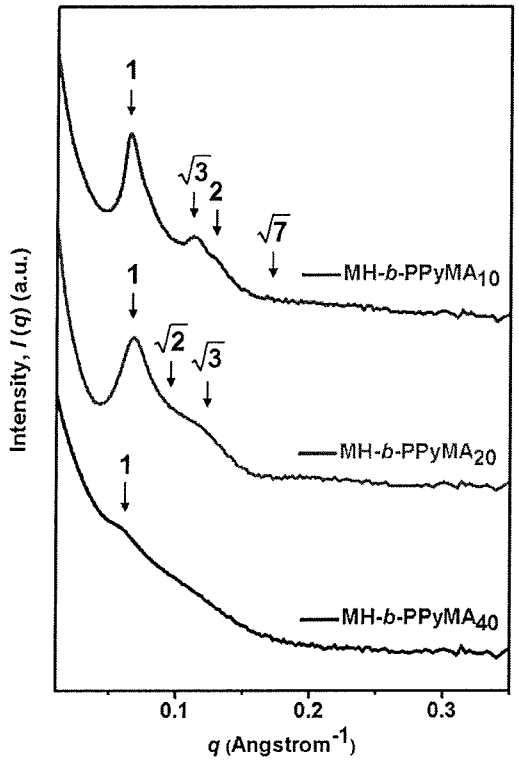

Fig. 4 1-D SAXS profiles of thermo-annealed MH-*b*-PPyMA bulk samples.

(~4.3 nm) and $PPyMA_{40}$ (~5.9 nm) blocks, though $PPyMA_{10}$ has the shortest chain length, which indicates that the $PPyMA_{10}$ block is more stretched at the interface when it self-assembles. Notably, according to the phase-separation theory of a block copolymer, the order–disorder phase transition strongly depends on the χN value; if the N value is decreased, the χ value should be increased in order to maintain enough driving force for microphase separation. It is amazing that the total N = 17 of MH-*b*-$PPyMA_{10}$ is enough for phase separation compared to the previous cases that MH-*b*-PTMSS requires a smallest N of 22 [35] and MH-*b*-PS of N = 43.[36] This seems to suggest that the strong intermolecular interaction between bulky pyrenyl moieties helps to facilitate the phase separation. Transmission electron microscopy (TEM) measurements were also carried out to investigate the morphologies, while no clear nanostructures have been observed due to the poor selectivity of staining agents.

Apart from the morphology of bulk samples, the morphology of MH-*b*-PPyMA thin films is also studied by atomic force microscopy (AFM) and grazing incidence small-angle X-ray scattering (GISAXS). In the AFM images shown in Fig. S9 (ESI†), the obvious spherical aggregates are observed in as-cast films with a root-mean-square (RMS) surface roughness of 0.653–1.279 nm; after the thermal annealing process, the annealed thin films have a reduced RMS of 0.337–0.664 nm, implying that the annealing process has effectively facilitated the polymer chain relaxation and ameliorated the arrangement of the polymer chains. An increase of roughness with increasing PPyMA chain length is observed, due to more irregular packing caused by the enhancement of chain stiffness and strong molecular interactions between PPyMA blocks. Unfortunately, after the annealing process only spherical nano-aggregations are observed. To further obtain the morphological information on MH-*b*-PPyMA thin films, the GISAXS measurements were carried out, as shown in Fig. S10 (ESI†). In the 2-D GISAXS scattering patterns, the diffraction spots only appeared along the q_y axis; the 1-D q_y scanning plots (Fig. S11 (ESI†)) of the MH-*b*-PPyMA thin films show clear first-order peaks, while no distinct higher-order peak has been observed. Hence, we cannot judge the self-assembled structure of thin films from these GISAXS data. Considering the SAXS results of the bulk samples, the morphologies are assumed to be nano-spherical structures for MH-*b*-$PPyMA_{20}$ and MH-*b*-$PPyMA_{40}$ thin films, but not for MH-*b*-$PPyMA_{10}$ thin films. The reason for the morphological difference of MH-*b*-$PPyMA_{10}$ in its bulk and thin film state is likely due to some unclear factors like hydrophilic/hydrophobic interactions, surface energy, and intermolecular interactions. The hydrophilic MH moiety with strong hydrogen bonding and high surface energy is much likely to be surrounded by the PPyMA shell with phase separation proceeding. This core–shell structure is extremely stable so that it remains even after the annealing process is implemented. Therefore, only a spherical nanodomain is observed in the MH-*b*-$PPyMA_{10}$ thin films due to its high content of MH segments. Although GISAXS measurements do not provide precise structural information on the MH-*b*-PPyMA thin films, the *d*-spacing can still be estimated from the scattering vector of the primary reflection. The *d*-spacing values are calculated to be 7.8 and 8.4 nm for the as-cast and thermo-annealed MH-*b*-$PPyMA_{10}$ films, 8.3 and 8.5 nm for MH-*b*-$PPyMA_{20}$ films, and 10.1 and 10.4 nm for MH-*b*-$PPyMA_{40}$ films, respectively. The larger *d*-spacing of the thermo-annealed MH-*b*-PPyMA film again indicates that the annealing process is an efficient way to improve the molecular arrangement.

Morphology of the thin film

The supramolecular MH(4Py-Acceptor-4Py)$_x$-*b*-PPyMA is prepared by hydrogen-bonding a fixed amount of 4Py-Acceptor-4Py to the hydroxyl groups of MH segments. The subscript "*x*" stands for the molar ratio between 4Py-Acceptor-4Py and hydroxyl group; the "Acceptor" represents either 2,1,3-benzothiadiazole (BT) or *N*,*N*′-bis(2-octyldodecyl)-isoindigo (IID). Fig. S12 (ESI†) shows the FT-IR spectra of free 4Py-Acceptor-4Py and the MH(4Py-Acceptor-4Py)$_x$-*b*-PPyMA thin films. In contrast to the absorption bands of pyridyl groups of 4Py-Acceptor-4Py at 993 cm^{-1} and 1599 cm^{-1}, the hydrogen-bonded pyridyl groups in MH(4Py-Acceptor-4Py)$_x$-*b*-PPyMA show the peak shifting to 1001 cm^{-1} and 1605 cm^{-1}, respectively, indicating the supramolecular formation.[37] AFM images in Fig. 5 and S13 (ESI†) show the surface morphologies of the thermo-annealed MH(4Py-Acceptor-4Py)$_x$-*b*-PPyMA thin films.

 This journal is © The Royal Society of Chemistry 2016

Published on 09 December 2015. Downloaded by National Tsing Hua University on 27/06/2016 03:03:47.

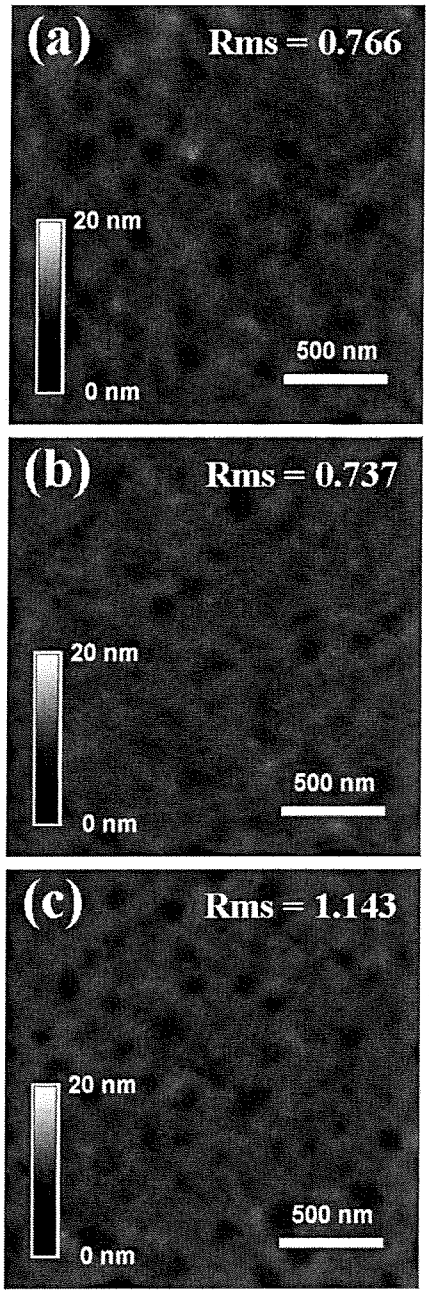

Fig. 5 AFM images of the surfaces of the thermo-annealed MH(4Py-Acceptor-4Py)$_x$-*b*-PPyMA$_n$ thin films (electret layers): (a) MH(4Py-BT-4Py)$_{1.0}$-*b*-PPyMA$_{10}$, (b) MH(4Py-BT-4Py)$_{1.0}$-*b*-PPyMA$_{20}$, and (c) MH(4Py-BT-4Py)$_{1.0}$-*b*-PPyMA$_{40}$.

Only spherical nano-aggregates are seen as the same as those in MH-*b*-PPyMA thin films, though their phase transformation has been expected because the incorporation of 4Py-Acceptor-4Py into the MH segment would reduce the hydrogen-bonding interaction between MH blocks, decrease the surface energy by increasing the hydrophobicity, and increase the volume fraction of the MH block. However, no apparent cylindrical or lamellar nanostructures are observed in the thermo-annealed MH(4Py-Acceptor-4Py)$_x$-*b*-PPyMA thin films. A reasonable explanation is that the 4Py-Acceptor-4Py with two pyridyl groups can form hydrogen-bonds with hydroxyl groups from different MH segments, leading to a physical cross-linking effect and rather strong interaction between MH segments. The RMS roughness of the thermo-annealed MH(4Py-Acceptor-4Py)$_x$-*b*-PPyMA thin-film surface is also analyzed. Obviously, the RMS roughness of supramolecular films (0.494–1.198 nm) is much greater than their precursor MH-*b*-PPyMA thin films (0.337–0.664 nm); the RMS roughness increases with increasing the content of 4Py-BT-4Py, indicating the formation of more aggregates. This is evidence that the incorporation of 4Py-Acceptor-4Py facilitates the aggregation of MH blocks. We further carried out 2-D GISAXS in order to investigate the surface morphologies of the MH(4Py-Acceptor-4Py)$_x$-*b*-PPyMA thin films, as shown in Fig. S14 (ESI†). Compared to the previous results on the pristine MH-*b*-PPyMA films, the weaker scattering signal suggests poorer periodic structures formed in MH(4Py-Acceptor-4Py)$_x$-*b*-PPyMA thin films. From the 1-D q_y scanning plots in Fig. S15 (ESI†), the average *d*-spacing can be estimated from the first-order scattering peak, which is calculated to be 9.6, 9.7, and 9.0 nm for MH(4Py-BT-4Py)$_{1.0}$-*b*-PPyMA$_{10}$, MH(4Py-BT-4Py)$_{1.5}$-*b*-PPyMA$_{10}$, and MH(4Py-IID-4Py)$_{1.0}$-*b*-PPyMA$_{10}$, 9.5, 9.5, and 8.5 nm for MH(4Py-BT-4Py)$_{1.0}$-*b*-PPyMA$_{20}$, MH(4Py-BT-4Py)$_{1.5}$-*b*-PPyMA$_{20}$, and MH(4Py-IID-4Py)$_{1.0}$-*b*-PPyMA$_{20}$, and 11.7, 11.6, and 10.7 nm for MH(4Py-BT-4Py)$_{1.0}$-*b*-PPyMA$_{40}$, MH(4Py-BT-4Py)$_{1.5}$-*b*-PPyMA$_{40}$, and MH(4Py-IID-4Py)$_{1.0}$-*b*-PPyMA$_{40}$ thin films, respectively. Compared to the size of nano-aggregates in the MH(4Py-Acceptor-4Py)$_x$-*b*-PPyMA thin film, the *d*-spacing after incorporating 4Py-Acceptor-4Py increases, which in turn supports the formation of MH(4Py-Acceptor-4Py)$_x$-*b*-PPyMA supramolecules.

Morphology of the pentacene layer on MH(4Py-Acceptor-4Py)$_x$-*b*-PPyMA electrets

On the thermo-annealed MH(4Py-Acceptor-4Py)$_x$-*b*-PPyMA layer, a semiconductor layer of pentacene is thermo-deposited; its surface information is examined by AFM, as shown in Fig. S16 (ESI†). The granular-shaped pentacene crystal is clearly observed, from which the grain size is estimated to be *ca.* 900 nm for those grown from the MH(4Py-BT-4Py)$_x$-*b*-PPyMA layers, 300–400 nm for those from MH(4Py-IID-4Py)$_{1.0}$-*b*-PPyMA$_{10}$ and MH(4Py-IID-4Py)$_{1.0}$-*b*-PPyMA$_{20}$, and 600–700 nm for that from the MH(4Py-IID-4Py)$_{1.0}$-*b*-PPyMA$_{40}$ layer, respectively. The grain size of the pentacene crystal grown from the MH(4Py-IID-4Py)$_x$-*b*-PPyMA layer is obviously smaller than that from the MH(4Py-BT-4Py)$_x$-*b*-PPyMA layer. This is because the bulky isoindigo induces more disordered molecular packing of PPyMA blocks due to the mutual π–π stacking between isoindigo moieties and PPyMA blocks. This inference is confirmed by the 2-D grazing incidence wide-angle X-ray scattering (GIWAXS) data shown in Fig. S17 (ESI†). The obvious diffraction spots are observed in two directions, q_y and q_z, which are assigned to the in-plane and out-of-plane signals of pentacene crystals, respectively. The dot-like

Published on 09 December 2015. Downloaded by National Tsing Hua University on 27/06/2016 03:03:47.

diffraction patterns suggest the formation of large grains of pentacene crystals on the MH(4Py-BT-4Py)$_x$-*b*-PPyMA layer. The situation is just the opposite when pentacene crystals are grown from the MH(4Py-IID-4Py)$_x$-*b*-PPyMA layer. On the MH(4Py-IID-4Py)$_x$-*b*-PPyMA surface, pentacene crystals forming a bulk phase are apparent because the shape of the diffraction pattern for torsion-angle determination changes from dot-like to elliptic, indicating that the torsion-angle between pentacene molecules increases to form the less-ordered packing in pentacene thin films, *i.e.*, the small grain size.[38,39]

Optical and electrochemical properties

The optical and electrochemical properties of PPyMA-N_3, MH-*b*-PPyMA, and 4Py-Acceptor-4Py were characterized by UV-Vis and cyclic voltammogram (CV) measurements, as shown in Fig. 6 and S18 (ESI†) and summarized in Table 2. The absorption spectra of both PPyMA-N_3s and MH-*b*-PPyMAs show a very weak peak around 370–380 nm and two intense bands separately located in the regions of 300–360 and 220–290 nm, which are accordingly attributed to the state transitions of S_0 to S_1, S_0 to S_2, and S_0 to S_3, respectively. The weak feature at 375 nm is the symmetry-forbidden transition from the S_0 to S_1 state.[40] The optical band gaps ($E_g^{opt.}$) of PPyMA$_{10}$-N_3, PPyMA$_{20}$-N_3, PPyMA$_{40}$-N_3, MH-*b*-PPyMA$_{10}$, MH-*b*-PPyMA$_{20}$, MH-*b*-PPyMA$_{40}$, 4Py-BT-4Py, and 4Py-IID-4Py estimated from the onset wavelength (λ^{onset}) of the absorption spectra are 3.19, 3.19, 3.19, 3.18, 3.19, 3.19, 2.89, and 1.90 eV, respectively. Similarly to our previous report,[21] the existence of the MH segment in MH-*b*-PPyMA has no significant effect on the electronic characteristics of the PPyMA block since the $E_g^{opt.}$ of each PPyMA is almost the same as that of its corresponding MH-*b*-PPyMA. The smaller band gap of 4Py-IID-4Py than that of 4Py-BT-4Py suggests that the isoindigo with a longer conjugation length facilitates the π to π^* transition. The highest occupied molecular orbital (HOMO) energy levels of the polymer electrets were determined from the onset of oxidation waves in CV curves with reference to ferrocene (4.8 eV), while the lowest unoccupied molecular orbital (LUMO) energy levels were estimated from the difference between the optical band gap and the HOMO level. The estimated HOMO levels of PPyMA$_{10}$-N_3, PPyMA$_{20}$-N_3, PPyMA$_{40}$-N_3, MH-*b*-PPyMA$_{10}$, MH-*b*-PPyMA$_{20}$, and MH-*b*-PPyMA$_{40}$ are −5.69, −5.69, −5.68, −5.68, −5.67, and −5.68 eV, and their LUMO levels are −2.50, −2.50, −2.49, −2.49, −2.48, and −2.50 eV, respectively. The similar energy levels between each PPyMA-N_3 and its related MH-*b*-PPyMA again indicate that the MH block does not have a significant effect on the electrochemical reaction during redox processes. Similarly, the LUMO and HOMO levels of 4Py-Acceptor-4Py are also obtained by reduction curves in CV and their $E_g^{opt.}$s, the LUMO levels of 4Py-BT-4Py and 4Py-IID-4Py are −3.67 and

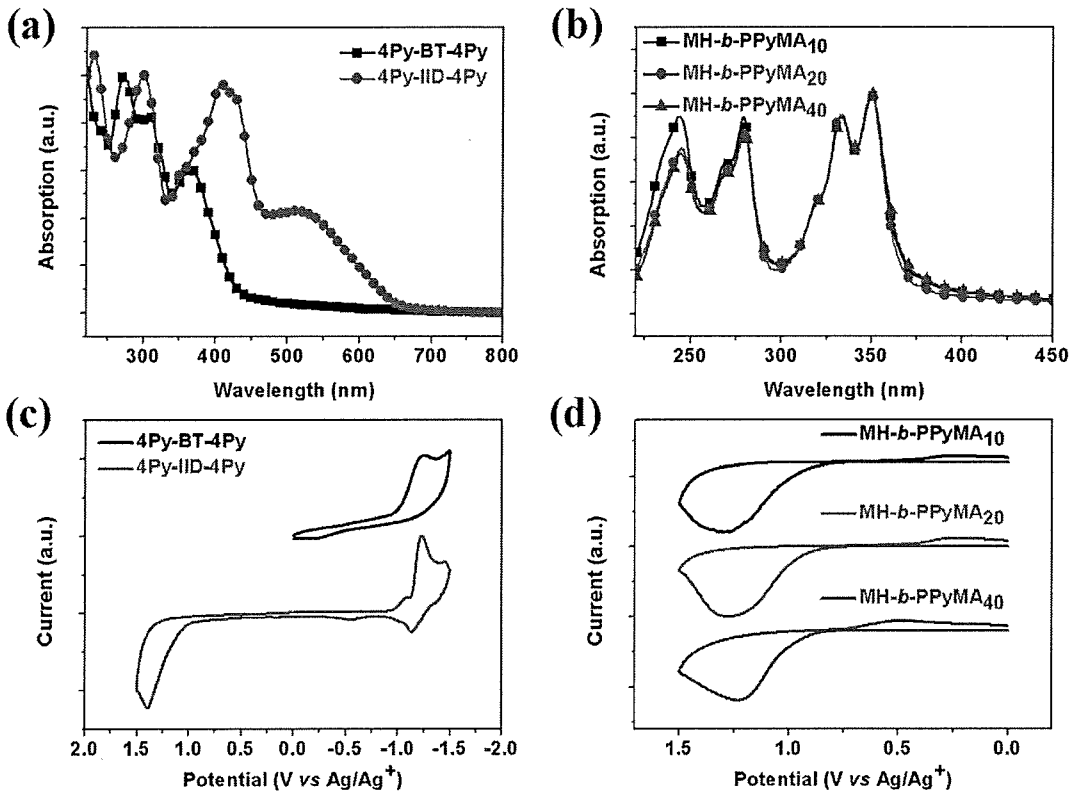

Fig. 6 Optical absorption and electrochemical properties of 4Py-Acceptor-4Py and MH-*b*-PPyMA diblock copolymers: (a) and (b) UV-Vis spectra; (c) and (d) cyclic voltammograms.

 This journal is © The Royal Society of Chemistry 2016

Published on 09 December 2015. Downloaded by National Tsing Hua University on 27/06/2016 03:03:47.

Table 2 Optical and electrochemical characteristics of 4Py-Acceptor-4Py, PPyMA$_n$-N$_3$ homopolymers, and MH-*b*-PPyMA$_n$ block copolymers[a]

Samples	E_g^{opt} [b] (eV)	HOMO/E_{onset}^{ox} [c] (eV/V)	LUMO/$E_{onset}^{red.}$ [c] (eV/V)	HOMO[d] (eV)	LUMO[d] (eV)
4Py-BT-4Py	2.89	n.a.[e]	−3.67/−1.02	−6.56	n.a.[e]
4Py-IID-4Py	1.90	−5.80/1.11	−3.74/−0.96	−5.64	−3.90
PPyMA$_{10}$-N$_3$	3.19	−5.69/0.99	n.a.[e]	n.a.[e]	−2.50
PPyMA$_{20}$-N$_3$	3.19	−5.69/0.99	n.a.[e]	n.a.[e]	−2.50
PPyMA$_{40}$-N$_3$	3.19	−5.68/0.98	n.a.[e]	n.a.[e]	−2.49
MH-*b*-PPyMA$_{10}$	3.18	−5.68/0.99	n.a.[e]	n.a.[e]	−2.49
MH-*b*-PPyMA$_{20}$	3.19	−5.67/0.98	n.a.[e]	n.a.[e]	−2.48
MH-*b*-PPyMA$_{40}$	3.19	−5.68/0.99	n.a.[e]	n.a.[e]	−2.50

[a] Spun-cast film from a chloroform solution onto a quartz or ITO substrate. [b] Optical energy band gap estimated from the onset wavelength (λ^{onset} (nm)) of the optical absorption using the formula: $E_g^{opt.} = 1240/\lambda^{onset}$ (nm). [c] The HOMO and LUMO energy levels were determined from the onset oxidation potential ($E_{onset}^{ox.}$) and the onset reduction potential ($E_{onset}^{red.}$), and estimated on the basis of the reference energy level of ferrocene (4.8 eV). The relative formula is HOMO (eV) = −eV($E_{onset}^{ox.} - E_{1/2}$ (ferrocene) + 4.8) and HOMO (eV) = −eV($E_{onset}^{red.} - E_{1/2}$ (ferrocene) + 4.8); $E_{1/2}$ (ferrocene) is 0.106. [d] The HOMO and LUMO energy levels were estimated by using the following equation: HUMO (eV) = LOMO − $E_g^{opt.}$ and LUMO (eV) = HOMO + $E_g^{opt.}$. [e] Not available.

−3.74 eV, and the HOMO levels are −6.56 and −5.64 eV (−5.80 eV as estimated from the oxidation potential in CV curves), respectively. The similar LUMO level of 4Py-Acceptor-4Py implies that BT and isoindigo have similar electron-accepting abilities.

OFET memory characterization

Prior to the discussion, it is worth emphasizing that all the electret layers of the polymer thin films used in this study are thermo-annealed and all the memory devices are fabricated into a bottom-gate/top-contact configuration using the aforementioned thermo-deposited p-type pentacene layer as the charge transport layer, the polymer thin-film layer as the electret layer (charge storage layer), and SiO_2 as the dielectric layer, as shown in Fig. 7(a). All the MH(4Py-Acceptor-4Py)$_x$-*b*-PPyMA-based devices show a typical p-type accumulation mode with well-defined linear and saturation regions (Fig. S19 (ESI†)) and their related OFET characteristics are listed in Table 3. The field-effect mobility (μ) of the pentacene layer in the saturation region is 0.72–0.81 cm^2 V^{-1} s^{-1} for the MH(4Py-BT-4Py)$_{1.0}$-*b*-PPyMA-based device, 0.95–1.08 cm^2 V^{-1} s^{-1} for the MH(4Py-BT-4Py)$_{1.5}$-*b*-PPyMA-based device, and 0.20–0.54 cm^2 V^{-1} s^{-1} for the MH(4Py-IID-4Py)$_{1.0}$-*b*-PPyMA-based device, respectively. The higher μ of the MH(4Py-BT-4Py)$_x$-*b*-PPyMA-based device than that of the MH(4Py-IID-4Py)$_{1.0}$-*b*-PPyMA-based one is assumed to be attributed to its larger grain size and better molecular packing of the pentacene crystals. In addition, an obvious enhancement of the μ value with increasing the 4Py-BT-4Py ratio has been observed, which is due to the increase of the charge transfer between the pentacene layer and the MH (4Py-BT-4Py)$_{1.5}$-*b*-PPyMA layer when a greater amount of BT was blended.[16,41] The initial threshold voltage (V_{TH}) and the ON/OFF current ratio (I_{ON}/I_{OFF}) of the devices in Fig. 8 are observed in the range of −3 to −2 V and 10^7–10^8, respectively. To further study the memory characteristics, the devices are operated applying a gate voltage (V_g) pulse to monitor the shifting of transfer curves. When the device is programmed by a positive gate pulse (V_g = 50 V, V_d = 0 V for 2 s), the entire transfer curve shifts toward the more positive direction, leading to a high-conductance state (ON state) at zero gate voltage (V_g = 0 V), referred to as the "writing" process. On the other hand, upon providing a reverse (negative) gate bias (V_g = −50 V, V_d = 0 V for 2 s), the transfer curve shifts reversely to the negative direction and results in a low-conductance state (OFF state) at V_g = 0 V, which serves as the "erasing" process. The shifting interval of the transfer curves after applying a writing and erasing gate bias is defined as the memory window (ΔV_{TH}).

Firstly, the memory characteristics of the devices using PPyMA$_n$-N$_3$ electret layers were examined in control experiments. The memory characteristics are shown in Fig. S20(a)–(c) (ESI†). All PPyMA$_n$-N$_3$-based devices similarly show the much greater negative (erasing) V_{TH}s of *ca.* −34 V than their positive (writing) V_{TH}s of ~−5 V, leading to the conclusion that the pyrenyl moieties are more preferred to trap hole carriers. In addition to the control devices, the memory characteristics of the devices using MH-*b*-PPyMA$_n$ polymer electrets are also shown in Fig. S20(d)–(f) (ESI†). The MH-*b*-PPyMA$_n$ devices also exhibit large erasing V_{TH}s of ~−30 V and writing V_{TH}s of ~−5 V, which are very similar to those observed in the PPyMA$_n$-N$_3$-based control devices. The 4 V smaller erasing V_{TH} of the MH-*b*-PPyMA$_n$-based device than the PPyMA$_n$-N$_3$-based one is likely due to the following explanation: on one hand, the incorporation of MH segments with strong hydrogen-bonding decreases the aggregation of PPyMA$_n$ blocks when the thin film is formed and thus results in a smoother surface with fewer defects (the RMS roughness of PPyMA$_n$ polymer surfaces is 0.405, 0.423 and 0.683 nm for n = 10 to 40, which is higher than its corresponding block copolymers); on the other hand, the MH blocks contact with the pentacene layer to play the role of an electron-trapping well. Considering that the MH blocks are embedded in PPyMA, their trapping ability should be reduced, which has been observed in the previously reported MH-*b*-PStFl$_n$-based devices. However, surprisingly, the memory characteristics of MH-*b*-PPyMA$_n$-based devices are significantly distinct from those of previously reported MH-*b*-PStFl$_n$-based devices, in which the charge trapping ability of MH-*b*-PStFl$_n$-based devices would be smaller than that of the

Published on 09 December 2015. Downloaded by National Tsing Hua University on 27/06/2016 03:03:47.

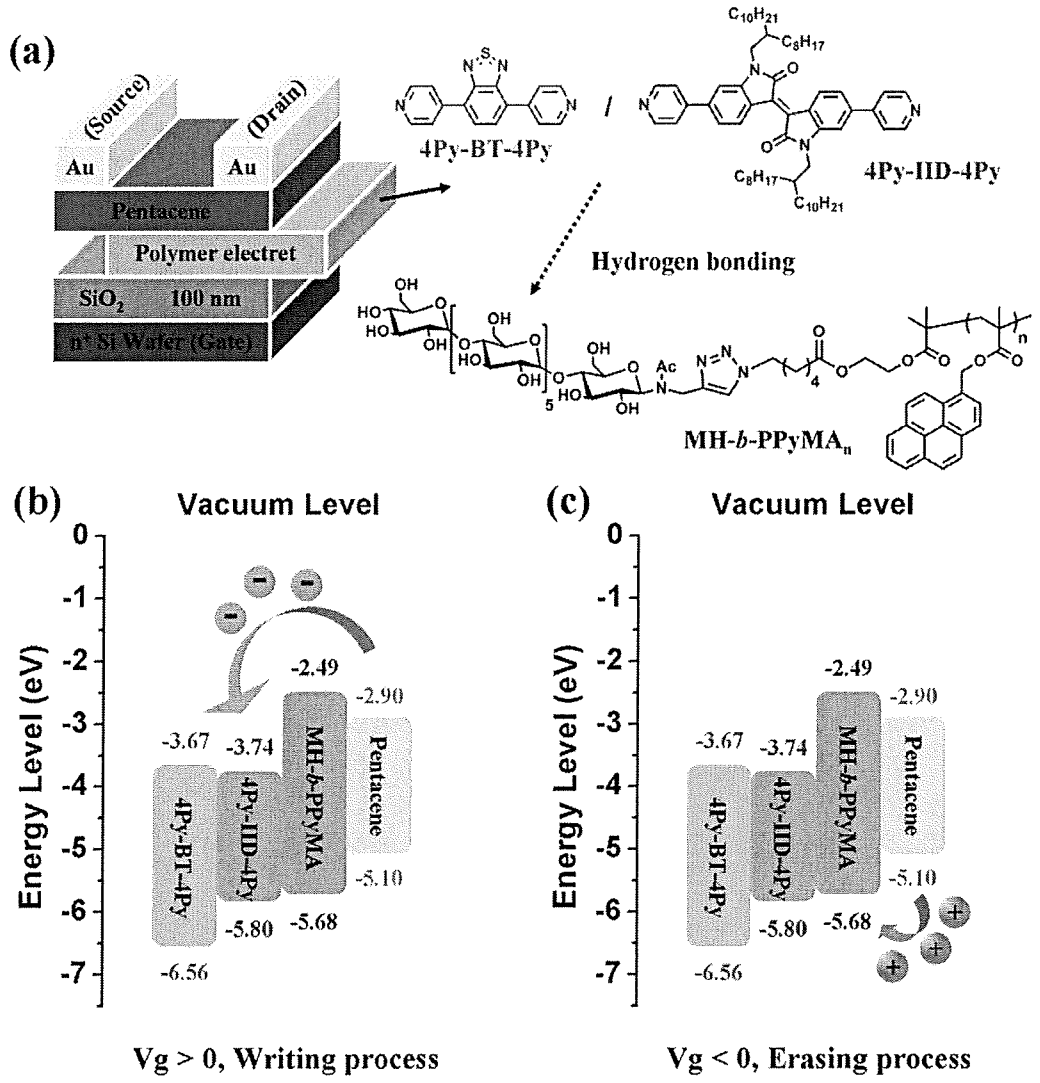

Fig. 7 The configuration of the studied transistor memory device (a) and memory mechanism of devices using thermo-annealed MH(4Py-Acceptor-4Py)$_x$-*b*-PPyMA$_n$ supramolecular electrets: (b) operation under positive gate voltage (writing process) and (c) operation under negative gate voltage (erasing process).

Table 3 OFET memory characteristics of the memory devices using the thermo-annealed MH(4Py-Acceptor-4Py)$_x$-*b*-PPyMA supramolecular electrets

Samples	μ [a] ($cm^2\ V^{-1}\ s^{-1}$)	$V_{TH,writing}$ (V)	$V_{TH,erasing}$ (V)	ΔV_{TH} [b] (V)
MH(4Py-BT-4Py)$_{1.0}$-*b*-PPyMA$_{10}$	0.73	7	−24	31
MH(4Py-BT-4Py)$_{1.0}$-*b*-PPyMA$_{20}$	0.72	2	−26	28
MH(4Py-BT-4Py)$_{1.0}$-*b*-PPyMA$_{40}$	0.81	−2	−27	25
MH(4Py-BT-4Py)$_{1.5}$-*b*-PPyMA$_{10}$	0.95	9	−25	34
MH(4Py-BT-4Py)$_{1.5}$-*b*-PPyMA$_{20}$	0.94	6	−27	33
MH(4Py-BT-4Py)$_{1.5}$-*b*-PPyMA$_{40}$	1.08	2	−27	29
MH(4Py-IID-4Py)$_{1.0}$-*b*-PPyMA$_{10}$	0.20	8	−28	36
MH(4Py-IID-4Py)$_{1.0}$-*b*-PPyMA$_{20}$	0.25	2	−29	31
MH(4Py-IID-4Py)$_{1.0}$-*b*-PPyMA$_{40}$	0.54	−3	−29	26

[a] Mobility was calculated from the saturation region and calibrated with the capacitance of polymer electrets. [b] ΔV_{TH} is defined as $V_{TH,erasing} - V_{TH,writing}$.

 This journal is © The Royal Society of Chemistry 2016

Published on 09 December 2015. Downloaded by National Tsing Hua University on 27/06/2016 03:03:47.

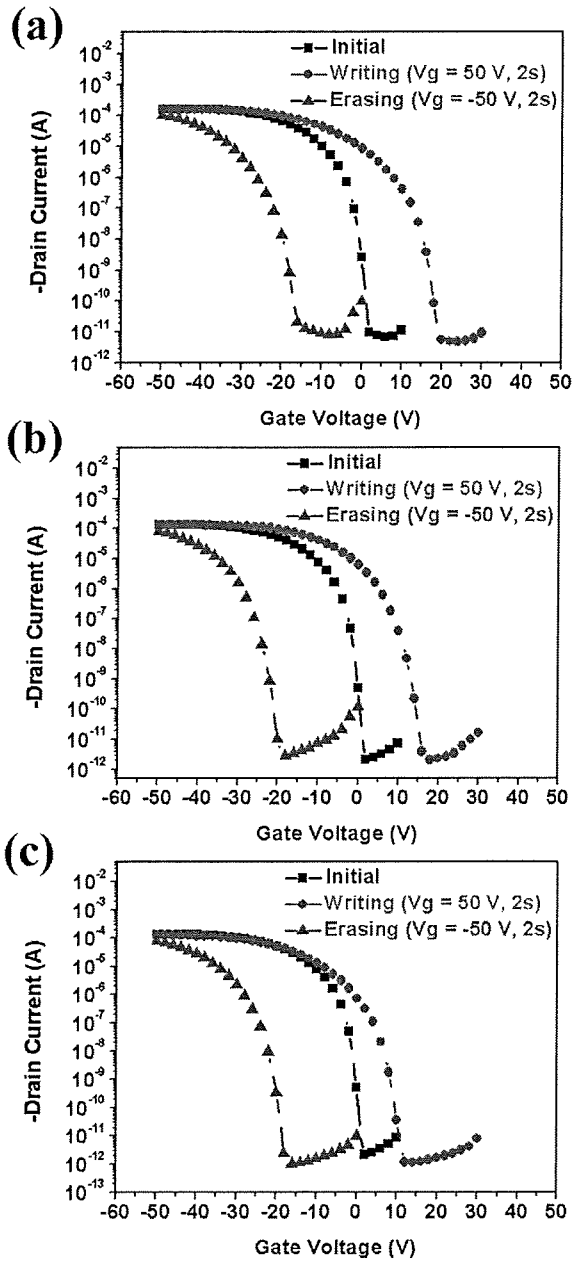

Fig. 8 The electric transfer curves of the memory devices using thermo-annealed MH(4Py-BT-4Py)$_{1.5}$-*b*-PPyMA$_n$ supramolecular electrets: (a) MH(4Py-BT-4Py)$_{1.5}$-*b*-PPyMA$_{10}$-based device, (b) MH(4Py-BT-4Py)$_{1.5}$-*b*-PPyMA$_{20}$-based device, and (c) MH(4Py-BT-4Py)$_{1.5}$-*b*-PPyMA$_{40}$-based device.

PStFl$_n$-based ones.[21] Given the fact that MH-*b*-PPyMA$_n$-based devices only trap holes, we believe that the reason for the MH-*b*-PPyMA$_n$-based device should be the same as that of the MH-*b*-PStFl$_n$-based device. Namely, the pyrenyl groups with greater molecular planes facilitate the formation of the densely-packed PPyMA$_n$ shell due to the strong π–π interaction, which leads to the increase of the electron injection barrier.

For precisely this reason, the 4Py-Acceptor-4Py has been added to improve the electron-trapping ability of the polymer electret layer. The memory characteristics of the MH(4Py-Acceptor-4Py)$_x$-*b*-PPyMA$_n$-based devices are shown in Fig. 8 and S21 (ESI†) and the detailed information is summarized in Table 3. After blending the BT acceptor, the MH(4Py-BT-4Py)$_{1.0}$-*b*-PPyMA$_{10}$-based device shows a writing V_{TH} of ~7 V and a memory window (ΔV_{TH}) of ~31 V, suggesting that the addition of 4Py-Acceptor-4Py effectively increases the electron-trapping ability of the polymer electret layer and also remarkably widens the ΔV_{TH}. The writing V_{TH} of the MH(4Py-BT-4Py)$_x$-*b*-PPyMA$_n$-based device increases with the increase of the blending ratio of 4Py-Acceptor-4Py, *e.g.*, ~9 V for the MH(4Py-BT-4Py)$_{1.5}$-*b*-PPyMA$_{10}$-based device and ~7 V for the MH(4Py-BT-4Py)$_{1.0}$-*b*-PPyMA$_{10}$-based one, while it decreases with the increase of PPyMA chain lengths. Both these phenomena should be caused by the change of the relative proportion of electron acceptors and donors. For MH(4Py-IID-4Py)$_x$-*b*-PPyMA$_n$-based devices, they have very similar memory characteristics to the MH(4Py-BT-4Py)$_x$-*b*-PPyMA$_n$-based ones except for a larger writing V_{TH} of ~8 V, which is due to the lower LUMO level of the isoindigo acceptor. A charge trapping mechanism for the MH(4Py-Acceptor-4Py)$_x$-*b*-PPyMA-based memory device is shown in Fig. 7(b) and (c), and is described as follows. Upon applying a positive gate electric field (the writing process), the negative charges are induced through pentacene from the source/drain electrode and are transferred into charge storage sites. Because of the suitable LUMO level of 4Py-Acceptor-4Py, the electron carriers are much more easily transferred to the 4Py-Acceptor-4Py by a tunneling effect and then trapped inside, leading to a profound positive shift of V_{TH} and a high conductance state (ON state) at V_g = 0 V. The p-type nature of the PPyMA$_n$ matrix with a thin thickness, which serves as the tunneling layer, enhances the built-in electric field and prevents the leakage of the induced electrons even after removing the external gate voltage,[1] which leads to the stabilization of the retention characteristics. For the erasing process, when the negative gate pulse is applied, the trapped electron charges are transferred back to the channel or neutralized by the injected hole carriers, resulting in the transfer curve shifting to a negative region; the device therefore returns to a low-conductance state (OFF state) at V_g = 0 V. Notably, the induced holes can easily transfer from the pentacene layer to the polymer electret layer because the HOMO energy barrier between pentacene and PPyMA$_n$ is smaller. This feature leads to the greater erasing V_{TH}s even when the same V_g is applied.

Finally, the stability of MH(4Py-Acceptor-4Py)$_x$-*b*-PPyMA$_n$-based OFET memory devices was investigated and shown in Fig. 9(a) and S22 (ESI†). The long retention time of the ON and OFF states of the MH(4Py-BT-4Py)$_x$-*b*-PPyMA$_n$-based devices at V_g = 0 V is maintained for 10^4 s with the I_{ON}/I_{OFF} ratios at the level of 10^6–10^7. On the contrary, the MH(4Py-IID-4Py)$_x$-*b*-PPyMA$_n$-based devices exhibit a rather fast degradation of ON current so that they have poorer charge retention characteristics than that of the MH(4Py-BT-4Py)$_x$-*b*-PPyMA$_n$-based devices, likely because the poorer self-assembled structures in the

Published on 09 December 2015. Downloaded by National Tsing Hua University on 27/06/2016 03:03:47.

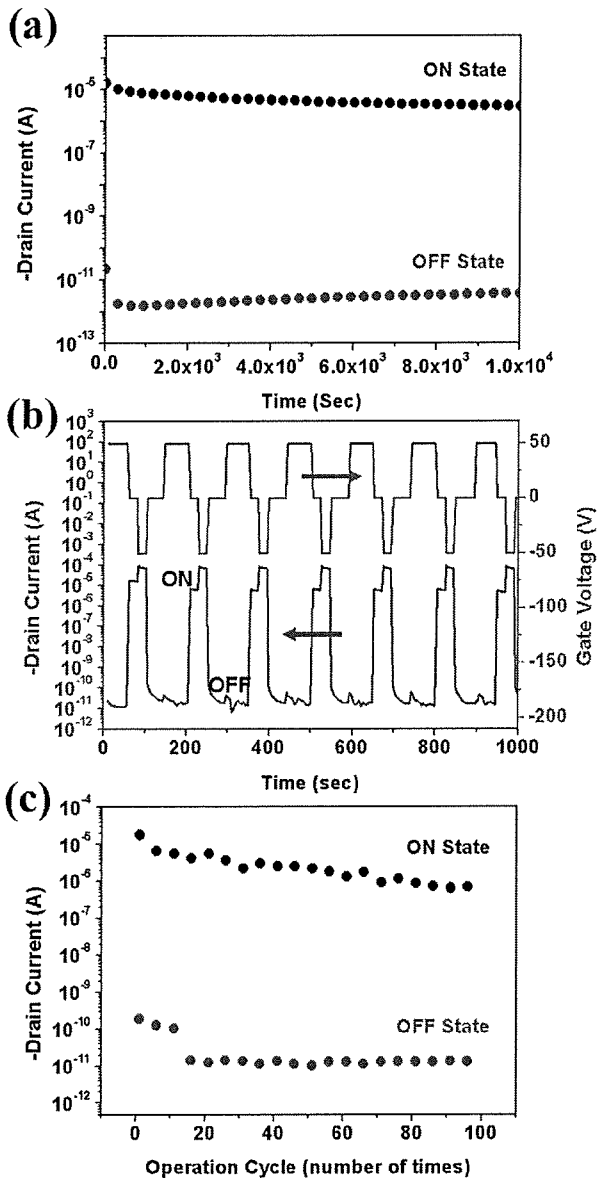

Fig. 9 The memory characteristics of the memory devices using thermo-annealed MH(4Py-BT-4Py)$_{1.5}$-*b*-PPyMA$_{10}$ supramolecular electrets: (a) the retention time curves, (b) the write–read–erase–read (WRER) cycles, and (c) the switching stability.

MH(4Py-IID-4Py)$_x$-*b*-PPyMA$_n$ thin films accelerate the leakage of trapped charges. These results indicate that the OFET memory device with the MH(4Py-BT-4Py)$_x$-*b*-PPyMA$_n$ electret is a more preferred candidate for the organic nonvolatile memory. The multiple switching stability of the devices using supramolecular electrets is further evaluated by using write–read–erase–read (WRER) cycles, as shown in Fig. 9(b) and S23 (ESI†). The operation conditions of WRER cycles are as follows: the drain current is kept at V_d = −30 V and the writing, reading, and erasing processes are implemented at V_g = 50, 0 and −50 V, respectively. Except for MH(4Py-Acceptor-4Py)$_{1.0}$-*b*-PPyMA$_{40}$-based devices, all other devices possess an I_{ON}/I_{OFF} ratio of around 10^4–10^5 for at least 100 cycles (Fig. 9(c) and S24 (ESI†)). The poor switching stability of MH(4Py-Acceptor-4Py)$_{1.0}$-*b*-PPyMA$_{40}$ devices can be considered as due to the much stronger accumulation of holes than that of electrons during the WRER measurement, because a large amount of hole-trapping pyrenyl moieties exists in the MH(4Py-Acceptor-4Py)$_{1.0}$-*b*-PPyMA$_{40}$ electret layer. The above results suggest that the performance of OFET memory devices can be greatly tuned by the composition of the acceptor and donor in a block polymer-based supramolecule.

Conclusions

Novel maltoheptaose-based diblock copolymers of MH-*b*-PPyMA have been successfully synthesized by the combination of the *t*-Bu-P$_4$-catalyzed GTP and the Cu(I)-catalyzed click reaction. For the thermo-annealed MH-*b*-PPyMA bulk samples, the sub-10 nm self-assembled nanomorphologies are observed. Their microphase separation in MH-*b*-PPyMA bulk samples can be controlled by the composition of MH and PPyMA segments. In addition, a cylindrical to spherical transformation of the nanostructure has been found with the increase of the DP of PPyMA from 10 to 40. For the thermo-annealed MH-*b*-PPyMA thin films, only spherical nanodomains have been seen due to the strong intermolecular interaction and high surface energy of MH. Compared with the control devices with ~50 nm thermo-annealed thin films of PPyMA-N$_3$ and MH-*b*-PPyMA as electret layers, the OFET memory devices using ~50 nm thermo-annealed thin films of MH(4Py-Acceptor-4Py)$_x$-*b*-PPyMA$_n$ as electret layers, except for the MH(4Py-Acceptor-4Py)$_{1.0}$-*b*-PPyMA$_{40}$ ones, exhibit excellent memory characteristics, *e.g.*, high I_{ON}/I_{OFF} ratios of 10^6–10^7, a long-term retention time larger than 10^4 s, and WRER cycles greater than 100. The results of this study provide a direct proof that the memory characteristics can be significantly tuned by the proportion of the acceptor and donor in a block copolymer-based supramolecule, and demonstrate the potential of the thermo-annealed MH(4Py-Acceptor-4Py)$_x$-*b*-PPyMA$_n$ thin film as the electret layer for non-volatile flash memory applications.

Acknowledgements

The authors are grateful to Mr. Naoya Kubota for experimental assistance in polymer synthesis and acknowledge the financial support from the Ministry of Science and Technology of Taiwan and Hokkaido University.

References

1 K. J. Baeg, Y. Y. Noh, H. Sirringhaus and D. Y. Kim, *Adv. Funct. Mater.*, 2010, **20**, 224–230.
2 Y. Yang, J. Ouyang, L. P. Ma, R. J. H. Tseng and C. W. Chu, *Adv. Funct. Mater.*, 2006, **16**, 1001–1014.

 This journal is © The Royal Society of Chemistry 2016

Published on 09 December 2015. Downloaded by National Tsing Hua University on 27/06/2016 03:03:47.

3 J. Li, H. S. Tan, Z. K. Chen, W. P. Goh, H. K. Wong, K. H. Ong, W. Liu, C. M. Li and B. S. Ong, *Macromolecules*, 2011, **44**, 690–693.
4 J. Li, Q. Bao, C. M. Li, W. Zhang, C. Gong, M. B. Chan-Park, J. Qin and B. S. Ong, *Chem. Mater.*, 2010, **22**, 5747–5753.
5 Y. H. Chou, H. C. Chang, C. L. Liu and W. C. Chen, *Polym. Chem.*, 2015, **6**, 341–352.
6 W. Wang, S. K. Hwang, K. L. Kim, J. H. Lee, S. M. Cho and C. Park, *ACS Appl. Mater. Interfaces*, 2015, 7, 10957–10965.
7 J. Hoffman, X. A. Pan, J. W. Reiner, F. J. Walker, J. P. Han, C. H. Ahn and T. P. Ma, *Adv. Mater.*, 2010, **22**, 2957–2961.
8 H. Y. Chi, H. W. Hsu, S. H. Tung and C. L. Liu, *ACS Appl. Mater. Interfaces*, 2015, 7, 5663–5673.
9 Y. C. Chiu, C. C. Shih and W. C. Chen, *J. Mater. Chem. C*, 2015, **3**, 551–558.
10 L. Dong, H. S. Sun, J. T. Wang, W. Y. Lee and W. C. Chen, *J. Polym. Sci., Part A: Polym. Chem.*, 2015, **53**, 602–614.
11 H. C. Chang, C. L. Liu and W. C. Chen, *ACS Appl. Mater. Interfaces*, 2013, 5, 13180–13187.
12 C. M. Chen, C. M. Liu, K. H. Wei, U. S. Jeng and C. H. Su, *J. Mater. Chem.*, 2012, **22**, 454–461.
13 C. C. Shih, Y. C. Chiu, W. Y. Lee, J. Y. Chen and W. C. Chen, *Adv. Funct. Mater.*, 2015, **25**, 1511–1519.
14 Y. H. Chou, S. Takasugi, R. Goseki, T. Ishizone and W. C. Chen, *Polym. Chem.*, 2014, **5**, 1063–1071.
15 J. C. Hsu, W. Y. Lee, H. C. Wu, K. Sugiyama, A. Hirao and W. C. Chen, *J. Mater. Chem.*, 2012, **22**, 5820–5827.
16 Y. C. Chiu, T. Y. Chen, C. C. Chueh, H. Y. Chang, K. Sugiyama, Y. J. Sheng, A. Hirao and W. C. Chen, *J. Mater. Chem. C*, 2014, **2**, 1436–1446.
17 Y. C. Chiu, I. Otsuka, S. Halila, R. Borsali and W. C. Chen, *Adv. Funct. Mater.*, 2014, **24**, 4240–4249.
18 M. Karakawa, M. Chikamatsu, Y. Yoshida, R. Azumi, K. Yase and C. Nakamoto, *Macromol. Rapid Commun.*, 2007, **28**, 1479–1484.
19 L. Valentini, M. Cardinali, E. Fortunati and J. M. Kenny, *Appl. Phys. Lett.*, 2014, 105.
20 K. Nagashima, H. Koga, U. Celano, F. Zhuge, M. Kanai, S. Rahong, G. Meng, Y. He, J. De Boeck, M. Jurczak, W. Vandervorst, T. Kitaoka, M. Nogi and T. Yanagida, *Sci. Rep.*, 2014, 4.
21 H.-S. Sun, Y.-C. Chiu, W.-Y. Lee, Y. Chen, A. Hirao, T. Satoh, T. Kakuchi and W.-C. Chen, *Macromolecules*, 2015, **48**, 3907–3917.
22 S. Malashikhin and N. S. Finney, *J. Am. Chem. Soc.*, 2008, **130**, 12846–12847.
23 J. You, J. A. Yoon, J. Kim, C. F. Huang, K. Matyjaszewski and E. Kim, *Chem. Mater.*, 2010, **22**, 4426–4434.
24 Y. Chen, K. Takada, N. Kubota, O. T. Eric, T. Ito, T. Isono, T. Satoh and T. Kakuchi, *Polym. Chem.*, 2015, **6**, 1830–1837.
25 C. Grandjean, A. Boutonnier, C. Guerreiro, J. M. Fournier and L. A. Mulard, *J. Org. Chem.*, 2005, **70**, 7123–7132.
26 S. Halila, M. Manguian, S. Fort, S. Cottaz, T. Hamaide, E. Fleury and H. Driguez, *Macromol. Chem. Phys.*, 2008, **209**, 1282–1290.
27 M. Akhtaruzzaman, M. Tomura, J. Nishida and Y. Yamashita, *J. Org. Chem.*, 2004, **69**, 2953–2958.
28 J. G. Mei, K. R. Graham, R. Stalder and J. R. Reynolds, *Org. Lett.*, 2010, **12**, 660–663.
29 J. C. Hsu, Y. G. Chen, T. Kakuchi and W. C. Chen, *Macromolecules*, 2011, **44**, 5168–5177.
30 U. S. Jeng, C. H. Su, C. J. Su, K. F. Liao, W. T. Chuang, Y. H. Lai, J. W. Chang, Y. J. Chen, Y. S. Huang, M. T. Lee, K. L. Yu, J. M. Lin, D. G. Liu, C. F. Chang, C. Y. Liu, C. H. Chang and K. S. Liang, *J. Appl. Crystallogr.*, 2010, **43**, 110–121.
31 L. W. Kroh, *Food Chem.*, 1994, **51**, 373–379.
32 L. W. Kroh, W. Jalyschko and J. Haseler, *Starch/Staerke*, 1996, **48**, 426–433.
33 K. Nakamura, T. Hatakeyama and H. Hatakeyama, *Polym. J.*, 1986, **18**, 219–225.
34 S. W. Kuo, H. Y. Xu, C. F. Huang and F. C. Chang, *J. Polym. Sci., Part B: Polym. Phys.*, 2002, **40**, 2313–2323.
35 J. D. Cushen, I. Otsuka, C. M. Bates, S. Halila, S. Fort, C. Rochas, J. A. Easley, E. L. Rausch, A. Thio, R. Borsali, C. G. Willson and C. J. Ellison, *ACS Nano*, 2012, **6**, 3424–3433.
36 K. Aissou, I. Otsuka, C. Rochas, S. Fort, S. Halila and R. Borsali, *Langmuir*, 2011, **27**, 4098–4103.
37 S. H. Tung, N. C. Kalarickal, J. W. Mays and T. Xu, *Macromolecules*, 2008, **41**, 6453–6462.
38 C. M. Chen, C. M. Liu, M. C. Tsai, H. C. Chen and K. H. Wei, *J. Mater. Chem. C*, 2013, **1**, 2328–2337.
39 P. Z. Jian, Y. C. Chiu, H. S. Sun, T. Y. Chen, W. C. Chen and S. H. Tung, *ACS Appl. Mater. Interfaces*, 2014, **6**, 5506–5515.
40 A. T. Haedler, H. Misslitz, C. Buehlmeyer, R. Q. Albuquerque, A. Köhler and H. W. Schmidt, *ChemPhysChem*, 2013, **14**, 1818–1829.
41 J. H. Kim, S. W. Yun, B. K. An, Y. D. Han, S. J. Yoon, J. Joo and S. Y. Park, *Adv. Mater.*, 2013, **25**, 719–724.